Complex 3D Migration and Delayed Triggering of Hydraulic Fracturing-Induced Seismicity

Honn Kao[1], Bei Wang[2], Dawei Gao[3], Ryan Visser[1], Ryan Schultz[4], and Rebecca M. Harrington[5]

[1]Geological Survey of Canada
[2]University of Victoria, Canada
[3]University of Victoria
[4]Stanford University
[5]Ruhr University Bochum

November 21, 2022

Abstract

Earthquakes resulting from hydraulic fracturing (HF) can have delayed triggering relative to injection commencement over a varied range of time scales, with many cases exhibiting the largest events near/after well completion. This poses serious challenges for risk mitigation and hazard assessment. Here, we document a high-resolution, three-dimensional source migration process with delayed mainshock triggering that is controlled by local hydrogeological conditions. Our results reveal that poroelastic effects might contribute to induced seismicity, but are insufficient to activate a non-critically stressed fault of sufficient size. The rapid pore-pressure build-up from HF can be very localized and capable of producing large, felt earthquakes on non-critically stressed fault segments. We interpret the delayed triggering as a manifestation of pore-pressure build-up along pre-existing faults needed to facilitate seismic failure. Our findings can deepen our understanding of the current stress state of crustal faults and also explain why so few injection operations are seismogenic.

Complex 3D Migration and Delayed Triggering of Hydraulic Fracturing-Induced Seismicity

Dawei Gao[1,2], Honn Kao[1,2]*, Bei Wang[1,2], Ryan Visser[2], Ryan Schultz[3], Rebecca Harrington[4]

[1]School of Earth and Ocean Sciences, University of Victoria, Victoria, British Columbia, Canada.

[2]Pacific Geoscience Centre, Geological Survey of Canada, Sydney, British Columbia, Canada.

[3]Department of Geophysics, Stanford University, Stanford, CA, USA.

[4]Ruhr University Bochum, Institute of Geology, Mineralogy, and Geophysics, Bochum, Germany.

*Corresponding author: Honn Kao (honn.kao@canada.ca)

Key Points:

- We document a complex 3D source migration process with delayed mainshock triggering that is controlled by local hydrogeological setting.
- Poroelastic effects might contribute to induced seismicity but are insufficient to activate a non-critically stressed fault of large size.
- Rapid pore-pressure build-up can be very localized and capable of producing large earthquakes on non-critically stressed fault segments.

Abstract

Earthquakes resulting from hydraulic fracturing (HF) can have delayed triggering relative to injection commencement over a varied range of time scales, with many cases exhibiting the largest events near/after well completion. This poses serious challenges for risk mitigation and hazard assessment. Here, we document a high-resolution, three-dimensional source migration process with delayed mainshock triggering that is controlled by local hydrogeological conditions. Our results reveal that poroelastic effects might contribute to induced seismicity, but are insufficient to activate a non-critically stressed fault of sufficient size. The rapid pore-pressure build-up from HF can be very localized and capable of producing large, felt earthquakes on non-critically stressed fault segments. We interpret the delayed triggering as a manifestation of pore-pressure build-up along pre-existing faults needed to facilitate seismic failure. Our findings can deepen our understanding of the current stress state of crustal faults and also explain why so few injection operations are seismogenic.

Plain Language Summary

Fluid injection-induced earthquakes (IIE), especially the mainshocks, are often observed to occur near or after well completion. Such delayed triggering relative to injection commencement poses serious challenges for both regulators and the energy industry to establish an effective mitigation strategy for the potential seismic risk. In this study, we reveal a high-resolution, complex three-dimensional pattern of IIE migration in Fox Creek, Alberta, Canada. The observed first-outward-then-inward IIE sequence highlights the significance of hydrogeological networks in facilitating fluid pressure migration and the associated seismic failure. The detailed spatiotemporal distribution of IIE suggests that the effect of pore-pressure build-up from hydraulic fracturing (HF) can be very localized. The delayed triggering is a combined result from the fluid pressure migration and the current stress state of the hosting fault system away from the HF wells. The findings from this study also provide plausible explainations on why only a very limited number of fluid injections are seismogenic.

1. Introduction

Fluid injection-induced earthquakes (IIE), especially relatively large ones, are often observed to have delayed triggering relative to injection commencement. For long-term wastewater disposal (WD), the delay time can be as long as decades (*Keranen et al*., 2013). For relatively short-term hydraulic fracturing (HF) operations, the delay time varies from days to weeks. In many cases, the largest events occur near or after well completion (*Schultz et al*., 2015a, 2015b, 2017, 2020; *Schultz and Wang*, 2020; *Lei et al*., 2017; *Igonin et al*., 2020; *Wang et al*., 2020; *Peña-Castro et al*., 2020) which severely challenges the designing of effective risk mitigation strategy. Understanding the controlling factor(s) of delayed triggering of induced seismicity is of paramount importance. However, the underlying physics is surprisingly far from clear due to limited observations and/or incomplete injection databases.

The 2015 Mw 3.9 earthquake sequence near Fox Creek, Alberta, Canada is the first well-known delayed HF-induced case with a ~2-week gap between the stimulation completion and the mainshock. The local seismograph array data contributed by the industry enables precise determination of earthquake hypocentres in comparison to other induced seismicity studies which often rely on regional stations (*Bao and Eaton*, 2016). During the post-stimulation process, only ~7% of the injected fluids, in contrast to a typical value of ~50% in western Canada, were recovered, unambiguously indicating that a tremendous amount of fluid has leaked off into nearby fault zones (*Bao and Eaton*, 2016). Given the robust earthquake locations, comprehensive stimulation database, and large volume of fluid loss, the 2015 Fox Creek sequence provides a unique opportunity to infer the corresponding three-dimensional (3D) fluid migration process and the spatiotemporal interactions between the hosting structures and injected fluid at an unpreceded resolution.

According to *Bao and Eaton* (2016), the Coulomb stress change (ΔCFS) due to fracture opening and pore-pressure diffusion are responsible for the earlier events that occurred during the HF stimulation (referred to as the east sequence) and the delayed post-stimulation events (west sequence, including the Mw 3.9 strike-slip mainshock), respectively (Figure 1a). However, this model has at least two serious issues. First, it is inconsistent with the observed chronological sequence of stimulation and seismicity. There are two periods of stage stimulation from north to south with a ~1-week gap (Figure 1). The earliest event (i.e., the east sequence) actually occurred about 2 days after the last stage of the first stimulation period (P1 in Figure 1b). This is contradictory to their assumed elastic stress triggering mechanism, which should be instantaneous. Instead, the 2-day delay suggests that pressure migration might have begun during or shortly after P1. Moreover, the west sequence seems to initiate at greater depth relative to the injection well with a clear upward trend of propagation (*Bao and Eaton*, 2016). Hence it is very unlikely that the west sequence was caused by fluids from the wellbore directly above (Figure 1a).

Second, the initial model results in an overestimation of static ΔCFS in triggering the earlier events (east sequence). The sudden increase of seismicity of the east sequence (including an Mw 3.2 earthquake) happened halfway through the second stimulation period (P2 in Figure 1b), when the treatment approached the vertical fault hosting the seismicity sequence (stages 14 and 15 of well 2 in Figure 1a). Thus, the actual ΔCFS in triggering these events is significantly overestimated by simply summing the effects of all HF stages. Furthermore, the extremely large injected volume (~50% more) and long duration (~5.75 times longer) of stage 14 compared with other stages suggest the likely start time of serious fluid leakage (Figure 1b) (*Peña-Castro et al.*, 2020). Consequently, it is inappropriate to calculate the net ΔCFS by assuming that the total fracture (opening) volume equals the total volume of injected fluid (*Bao and Eaton*, 2016).

Here we revisit the 2015 Fox Creek sequence with tight constraints from local geological structures and injection parameters. We first employ waveform cross-correlation and hierarchical clustering analysis to identify near-identical events with highly similar waveforms. The distribution of these events is used to delineate the geometry of corresponding fault structures. We then analyse the spatiotemporal evolution of these on-fault near-identical events. By taking advantage of the complete stimulation database, we further conduct poroelastic modeling to investigate the delayed triggering process. Our results reveal a high-resolution, complex 3D pattern of IIE migration that is probably controlled by local fault architecture and its hydrogeological properties. Finally we discuss the broad implications of this study.

2. Methods

2.1 Waveform Cross-correlation and Hierarchical Clustering Analysis

Near-identical waveforms between events are commonly interpreted as indication of a similar source location and focal mechanism (*Schultz et al*., 2014). Here we directly adopt the high accuracy earthquake catalog (69 events in total) reported in the literature (*Bao and Eaton*, 2016) and perform pair-wise waveform cross-correlation and clustering analysis (*Schultz et al*., 2014, 2015, 2017; *Hayward and Bostock*, 2017) to identify near-identical events. The cataloged events were mainly determined by local seismograph array data contributed by the industry in addition to regional seismic stations and were relocated with hypoDD (*Bao and Eaton*, 2016).

The waveform similarity can be quantitatively characterized by cross-correlation coefficients (CC). Since data availability of the private seismograph array used by prior work (*Bao and Eaton*, 2016) is restricted, we choose to calculate the CC values between event pairs with seismograms from the station BRLDA (Figure 1a) that have a generally high signal-to-noise ratio (*Schultz et al*., 2015, 2017) and are publicly accessible from Incorporated Research Institutions for Seismology (http://ds.iris.edu/ds/nodes/dmc/, last accessed July 2020). The technical details of CC calculation are presented in Text S1.

The aforementioned pair-wise cross-correlation yields a $[69\times 69]$ similarity matrix. We obtain the near-identical events by implementing a hierarchical clustering algorithm based on the unweighted pair-group method using the average approach (UPGMA), available as a SciPy package (*Jones et al*., 2001, https://docs.scipy.org). Compared with the "chain-like" methods (e.g., *Igarashi et al*., 2003), the UPGMA method yields more robust results in grouping earthquakes (*Hayward and Bostock*, 2017). Here we define a cluster as a group of events in which the CC of all pairs are higher than 0.75 (Figure 2a). Such a CC threshold, the same as the value used in other IIE related clustering studies (e.g., *Schultz et al*., 2014; *Cauchie et al*., 2020), is determined by visually inspecting the waveforms in the corresponding cluster. Eventually, we obtain 1 cluster with 20 near-identical events. The high similarity of the event waveforms, including the coda train, justifies our choice of the threshold value (Figure 2b).

2.2 Poroelastic Modeling and *ΔCFS* Calculation

To investigate the predominant triggering mechanism, we conduct poroelastic modeling that takes into account the interaction between pore pressure change (ΔP) and rock matrix deformation. We use the COMSOL Multiphysics® software (version 5.3a) to model the evolution of pore pressure and poroelastic stress surrounding the two HF horizontal wells. COMSOL Multiphysics® software employs the finite-element algorithm to simulate the fluid-solid coupling in a realistic scenario, thus we can estimate the pore pressure and poroelastic stress simultaneously. In this study, we apply the solid mechanism module and Darcy's fluid flow module to simulate the coupling process. The technical details of poroelastic modeling are given in Text S2.

The ΔCFS has been commonly used to study the earthquake triggering process (e.g., *Stein*, 1999; *Deng et al*., 2016). After we obtain the stress tensor and pore pressure change from the COMSOL model, then we use the following equation to calculate the ΔCFS resolved on the specific fault plane (*Xu et al*., 2010):

$$\Delta CFS = \sin\lambda \left[\frac{-1}{2} s\text{¿}^2 \phi \sin(2\tilde{\delta})\sigma^{11} + \frac{1}{2}\sin(2\phi)\sin(2\tilde{\delta})\sigma^{12} + \sin\phi\cos(2\tilde{\delta})\sigma^{13} - \frac{1}{2}\cos^2\phi\sin(2\tilde{\delta})\sigma^{22} - \cos\phi\sin(2\tilde{\delta}) \right.$$

(1)

where $\mu = 0.6$ is the friction coefficient, ϕ, $\tilde{\delta}$, and λ are the strike, dip, and rake of the receiver fault, respectively, σ^{ij} is the stress tensor, where i, j = 1, 2, 3 are the 3D components in the Cartesian coordinate system, and ΔP is the pore pressure change. Based on the Coulomb failure criteria, seismic slip is promoted for a positive ΔCFS, and vice versa (*King et al*., 1994).

3. Results

3.1 A High-resolution 3D Pattern of IIE Migration

Based on the results of waveform analysis (Section 2.1), 20 out of 69 events are found with high CC (>0.75) and near-identical waveforms, implying that they have ruptured on similar structures with similar focal mechanisms. Overall, the similarity matrix of these near-identical events shows two high CC patches (Figure 2a) – one corresponds to the earlier events in the east sequence and the other to the later events in the west sequence (Figure 3). Such a two-patch pattern is consistent with the two main near-vertical fault structures (Figure 3) inferred from earthquake focal mechanisms (*Schultz et al*., 2017). According to the "flower structure" model, these two near-vertical faults may merge together in the basement (*Wang et al*., 2017). The remaining 49 poorly correlated events are generally small (overall Mw ≤ 1, Figure S1) and likely to have occurred on the nearby tiny fractures with possibly different orientations and/or focal mechanisms.

It is worth noting that the event magnitudes increase with focal depth for both the east and west sequences (Figure 3). The overall pattern of relative location among hypocenters should be very robust as they are determined by the high-resolution double-difference method (*Waldhauser and Ellsworth*, 2000) with data from a local seismic array established by the private industry (*Bao and Eaton*, 2016). Most of the largest events appear to have occurred near/in the crystalline basement, possibly due to the varied degrees of fault maturity at different depths (*Kozłowska et al.*, 2018). In comparison, there is no significant event immediately above or below the HF-targeted Duvernay shale formation (Figure 3). It appears that the aseismic region can extend up to 200 m surrounding the horizontal wells (*Guglielmi et al*., 2015; *Eyre et al*., 2019a).

The spatiotemporal evolution of the near-identical on-fault events (colored circles in Figure 3) clearly shows how the seismicity migrates in a 3D way: first in the east from shallow to deep, then shifting to the west, finally from deep to shallow. The seismicity migration, along with the huge fluid loss (*Bao and Eaton*, 2016), inherently implies the migration of the leaked fluid along pre-existing geological faults. Although the east sequence falls out of the target fracturing region (which is usually within a few hundred meters of the well), it is highly likely that a direct fluid connection exists between the injection well and triggered seismicity through permeable pathways. Such an inference is supported by many other cases documented in the literature (e.g., *Wolhart et al*., 2005; *Davies et al*., 2013; *Galloway et al.*, 2018; *Igonin et al*., 2020) where the maximum fluid communication distance can be as far as ~1 km (*Wilson et al*., 2018; *Igonin et al*., 2020; *Fu and Dehghanpour*, 2020). The uppermost part of the east sequence fault seems to be aseismic, possibly due to the close proximity to the injection area (*Guglielmi et al*., 2015; *De Barros et al*., 2016) and/or high clay and organic content in the shale formation that favors stable sliding (*Kohli and Zoback*, 2013; *Eyre et al*., 2019a). Upon fluid injection, the fault permeability in the vicinity of fluid channel may increase dramatically during the aseismic period (*Guglielmi et al*., 2015) which, in turn, facilitates rapid downward fluid pressure migration, eventually leading to seismic failures towards the basement. The fluid then migrates from east to west through faults in the basement as evident from the timing and location of the induced seismicity. Finally the fluid pressure may migrate vertically (*Birdsell et al*., 2015) along the west sequence fault hinted by the seismicity pattern (*Haagenson and Rajaram*, 2020). A lack of typical Omori-type aftershock sequences after the Mw 3.9 event on the west sequence fault (*Bao and Eaton*, 2016) provides another piece of evidence of the involvement of an external force (fluid pressure) (*Lei et al., 2017*; 2019) and thus explains the fluid's origin (from the east) and upward earthquake migration on the west.

In summary, in contrast to the conventional wisdom that the geomechanical effects due to fluid injection migrate outward from the injection site, our results reveal a high-resolution, complex 3D pattern of IIE migration that can go both outward and inward as controlled by local fault architecture and its hydrogeological properties. The pore pressure build-up due to rapid fluid pressure migration has caused the Mw 3.2 earthquake on the east sequence fault and Mw 3.9 event on the west (Figure 3). This first-outward-then-inward sequence highlights the significance of hydrologic networks in facilitating fluid pressure migration and the associated seismic failure. However, event No. 1 (Mw 1.98) appears to be an exception. It occurred very early (soon after the start of stage 17 of well 2 in P2, Figure 1b), not on the east sequence fault but on the west. The hypocenter is close to event No. 11 as evident by both high CC values (Figure 2a) and precise hypocentre locations (Figure 3). Given the timing and location, event No. 1 may have been caused by poroelastic effects rather than a pore pressure perturbation.

3.2 Delayed Triggering Due to Pore Pressure Build-up

We verify the hypothesis of the pore pressure build-up being the predominant triggering mechanism through poroelastic modeling (Section 2.2). In the model, we consider two scenarios for the east sequence fault: one where the near-vertical east sequence fault intersects the inferred horizontal fluid channel, and the other where it does not (Figure 3). Our model results indicate that the ΔCFS due to poroelastic effects alone (i.e., without hydrologic communication) is only ~0.06 bar (Figure 4a). Such a small change is likely insufficient to trigger the Mw 3.2 event on the east sequence fault as it is significantly below the triggering threshold (0.2 bar) adopted by previous studies (e.g., *Fischer et al*., 2008; *Wang et al*., 2021). Instead, allowing fluid pressure migration to the seismogenic east sequence fault can explain the observations very well. Figure 4a clearly shows that the ΔP dominates the ΔCFS in elevating stress to sufficient levels to cause the Mw 3.2 event. We also tested a range of physically reasonable permeability values (*Cappa*, 2009; *Farrel and Taylor*, 2014) for the inferred near-horizontal basement fault that facilitates rapid fluid pressure migration from the east sequence fault towards the west. A minimum permeability of 4×10^{-14} m^2, about 4 orders higher than that of the low-permeability country rock (10^{-18} m^2, Table S1), is found to be required to cause seismic failures on the west sequence fault for the observed time scale (Figure 4b). Such a high permeability value is consistent with the laboratory results of well-developed fault damage zones ($10^{-16} - 10^{-14}$ m^2) that lead to rapid fluid flow (*Evans et al*., 1997). Thus, we conclude that the pore pressure build-up associated with fluid pressure migration is the key mechanism that triggered the 2015 Fox Creek earthquake sequence, and that the complex 3D spatiotemporal pattern of hypocenters is dictated by the local hydrogeological setting. Our results also demonstrate that local hydrological pathways, fault structures, and a complete stimulation database (e.g., accurate stage timing and volume) must all be properly incorporated in the modeling to avoid incorrect outcomes and misinterpretation (*Bao and Eaton*, 2016).

4. Interpretation and Implications

4.1 Reactivation of A Non-critically Stressed Fault Segment

Previous studies have suggested that the hosting fault must be critically stressed for relatively large (M>2) IIE to occur (*Atkinson et al.*, 2020). However, our observations suggest that the east sequence fault was not critically stressed before stimulation, as no event was triggered by poroelastic effects when the stage stimulation started. Instead, the largest event in the east sequence (event No. 7) occurred ~3 days after event No. 0 (Fiugure 1b). The ~3-day delay time suggests that stage stimulation can dramatically alter the stress state from non-critical to critical over an extremely short period (on the order of days), in contrast to the tectonic loading cycle (on the order of tens/hundreds of years).

Another hint of reactivating a non-critically stressed fault by HF comes from the west sequence fault that hosts the 2015 Mw 3.9 event. About one year later, another comparable-sized event (Mw 4.1) was also induced by HF slightly to the south (Figure 1a; *Wang et al.*, 2017; *Eyre et al.*, 2019a, b). These two events share near-identical focal mechanisms (Figure 1a) and waveforms (Figure 2b), have adjacent locations (epicenters less than 1.5 km apart, and similar depths within ~1 km; *Schultz et al.*, 2017, *Eyre et al.*, 2019b), and both occurred after the completion of HF operations with potentially significant fluid leakage (*Bao and Eaton*, 2016; *Eyre et al.*, 2019b). Thus, the two large events are most likely to have occurred on two adjacent segments of the same N-S striking fault. Having two nearby ruptures of limited size instead of rupturing the whole west sequence fault at once suggests that the hosting fault is well below the critical state. This inference is also supported by a recent slip tendency analysis (*Shen et al.*, 2019). Our observations indicate that the effect of HF stimulation can be very localized for a non-critically stressed fault given the relatively small injected volume. Therefore, it can only elevate the stress state of a limited segment of the hosting fault to facilitate seismic failure.

4.2 Current Stress State of Crustal Faults

Our observations clearly show that both the east and west sequence faults were not critically stressed before stimulation, as no large earthquakes occurred at the very beginning of stimulation and/or were caused by poroelastic effects. Furthermore, the west sequence fault hosted two large earthquakes of comparable size on neighbouring segments instead of rupturing the whole fault at once. Considering the facts that (i) most injection operations are not seismogenic (*Atkinson et al.*, 2016; *Schultz et al.*, 2017, 2020; *Rubinstein and Mahani*, 2015; *Weingarten et al.*, 2015), (ii) events triggered by poroelastic effects are usually of small magnitudes (*Deng et al.*, 2016; *Kozłowska et al.*, 2018; *Yu et al.*, 2019), (iii) the elevation of pore pressure is widely considered to be the primary cause of relatively large IIE (*Lei et al.*, 2019; *Peña-Castro et al.*, 2020; *Wang et al.*, 2021; *Schultz and Wang*, 2020), and (iv) for the majority of HF-induced IIE cases, the largest events often occur near or after well completion (*Schultz et al.*, 2015a, 2015b, 2017; *Schultz and Wang*, 2020; *Lei et al.*, 2017; *Igonin et al.*, 2020; *Wang et al.*, 2020; *Peña-Castro et al.*, 2020), we infer that the number of critically stressed, large intraplate faults should be very limited, and that reactivation of such faults requires sufficient pore-pressure accumulation.

4.3 Delayed Triggering of IIE

Taking advantage of the high-resolution distribution of hypocentres and complete HF stimulation database, our study reveals that a complex 3D source migration process with the delay of large earthquakes is controlled by the local hydrogeological setting. Numerical modeling demonstrates that poroelastic effects alone (i.e., without direct hydrological connection) are insufficient to activate the east sequence fault. Instead, the delayed occurrence of two relatively large events (i.e., Mw 3.2 and Mw 3.9) on the time scale of days to weeks can be well-explained by the pore-pressure build-up along the complex local fault system involving an initially outward path at the shallow depth and a later inward one at a greater depth. Although the actual fluid channel and fault architecture could be even more complicated than what we have assumed (Figure 3), our model succeeds in explaining the IIE migration process to the first order.

Therefore, the complexity of the hydrologic network determines whether and how fast the fluid can reach the fault; and the current stress state of the hosting fault determines how long it takes for pore-pressure build-up to facilitate seismic failure. This might explain why no large IIE thus far occur at the onset of HF stimulation. Instead, they tend to occur near the end of, or even after the stage stimulation with a wide range of time delays (*Schultz et al*., 2015a, 2015b, 2017; *Schultz and Wang*, 2020; *Lei et al*., 2017; *Igonin et al*., 2020; *Wang et al*., 2020; *Peña-Castro et al*., 2020).

4.4 Seismogenic vs. Aseismogenic Injection Operations

Direct fluid communication should be geologically rare (*Galloway et al*., 2018). Whether earthquakes can be triggered by an injection operation depends on: (i) the probability of connecting the injection to a pre-existing seismogenic fault, and (ii) whether the amount of injected fluid is sufficient to bring the fault to critical state. Even if direct fluid communication exists, the largest magnitude of triggered events will depend on both the dimension of the pre-existing fault and the cumulative volume of injected fluid (*Schultz et al.*, 2018). Meeting all these conditions may be statistically demanding, and thus can explain why the majority of seismogenic wells do not produce large felt IIE. This essentially agrees with the Gutenberg-Richter law that smaller earthquakes occur much more frequently than the larger ones.

5. Discussion and Conclusions

Waveform similarity has been a powerful seismological tool recently to study earthquake source characteristics (*Schultz et al*., 2014, 2020). While there are increasing evidences that waveform CC alone cannot reliably distinguish repeating earthquakes from neighboring events (e.g., *Ellsworth and Bulut*, 2018), nearly identical waveforms are useful in identifying nearby earthquakes with similar focal mechanisms. In fact, using single-station CC values to identify earthquakes with similar origins has been a common practice in previous studies, especially for areas with limited station availability (e.g., *Li and Richards*, 2003; *Schaff and Richards*, 2004; *Li et al*., 2011; *Buurman et al*., 2013; *Schultz et al*., 2014, 2015, 2017; *Yamada et al*., 2016; *Hayward and Bostock*, 2017; *Cauchie et al*., 2020; *Gao and Kao*, 2020). We have tried different CC threshold values in our hierarchical clustering analysis, and the results are all similar. Although our cross-correlation and clustering analysis are based on single-station data, the overall match of the similarity matrix of the near-identical events (Figure 2a) and their hypocenter locations (Figure 3) demonstrate the effectiveness of our approach.

We take a more conservative approach in the investigation of the predominant triggering mechanism of IIE by assuming a triggering threshold of $\Delta CFS = 0.2$ bar (e.g., *Fischer et al*., 2008; *Wang et al*., 2021). Some studies have considered a lower value of 0.1 bar to define the triggering threshold (e.g., *Stein*, 1999; *King et al*., 1994). Regardless which triggering threshold (0.1 or 0.2 bar) is used, the ΔCFS due to poroelastic effects alone is much smaller (0.06 bar, Figure 4a) and hence is insufficient to trigger the Mw 3.2 event on the east sequence fault. We conclude that the poroelastic effects are at most a contributor in triggering the Mw 3.2 mainshock, whereas rapid pore-pressure build-up through permeable pathways may play a more important role.

To summarize, our study reveals that (i) poroelastic effects of HF stimulation might contribute to the occurrence of IIE, but are insufficient to activate a non-critically stressed fault segment of sufficient size, (ii) the effect of HF can be very localized and non-critically stressed fault segments can produce large felt IIE with rapid pore-pressure build-up, and (iii) the spatiotemporal distribution of IIE can exhibit a very complicated 3D pattern depending on the specific local hydrogeological setting. Therefore, mapping pre-existing geological faults and avoiding direct hydrologic connection to them may be of paramount importance in mitigating short-term seismic hazard from IIE. Precise and accurate assessment of the state of stress of local fault systems is probably the key step in the strategy of maximizing the economic benefit of HF operations and minimizing the potential impact to the safety of local communities and infrastructure.

Acknowledgements

Insightful discussions with Fengzhou Tan, Ramin Mohammad Hosseini Dokht, Yajing Liu, and Stan Dosso are much appreciated. Waveform data used in this study were downloaded from the Incorporated Research Institutions for Seismology (http://ds.iris.edu/ds/nodes/dmc/, last accessed July 2020). Seismic data are processed with Obspy (*Beyreuther et al*., 2010). Figures are made with Matplotlib (*Hunter*, 2007) and Inkscape (https://inkscape.org). This study is partially supported by a University of Victoria Fellowship (DG), the Induced Seismicity Research Project of NRCan (HK), Geoscience BC (HK), and a NSERC Discovery Grant (HK). This paper is NRCan contribution 2021xxxx.

References

Atkinson, G. M., Eaton, D. W., & Igonin, N. (2020). Developments in understanding seismicity triggered by hydraulic fracturing. *Nature Reviews Earth & Environment*, 1-14.

Atkinson, G. M., Eaton, D. W., Ghofrani, H., Walker, D., Cheadle, B., Schultz, R., ... & Kao, H. (2016). Hydraulic fracturing and seismicity in the Western Canada Sedimentary Basin. *Seismological research letters*, *87*(3), 631-647.

Bao, X., & Eaton, D. W. (2016). Fault activation by hydraulic fracturing in western Canada. *Science*, *354*(6318), 1406-1409.

Beyreuther, M., Barsch, R., Krischer, L., Megies, T., Behr, Y., & Wassermann, J. (2010). ObsPy: A Python toolbox for seismology. *Seismological Research Letters*, *81*(3), 530-533.

Birdsell, D. T., Rajaram, H., Dempsey, D., & Viswanathan, H. S. (2015). Hydraulic fracturing fluid migration in the subsurface: A review and expanded modeling results. *Water Resources Research*, *51*(9), 7159-7188.

Buurman, H., West, M. E., & Thompson, G. (2013). The seismicity of the 2009 Redoubt eruption. *Journal of Volcanology and Geothermal Research*, *259*, 16-30.

Cappa, F. (2009). Modelling fluid transfer and slip in a fault zone when integrating heterogeneous hydromechanical characteristics in its internal structure. *Geophysical Journal International*, *178*(3), 1357-1362.

Cauchie, L., Lengliné, O., & Schmittbuhl, J. (2020). Seismic asperity size evolution during fluid injection: case study of the 1993 Soultz-sous-Forêts injection. *Geophysical Journal International, 221*(2), 968-980.

Davies, R., Foulger, G., Bindley, A., & Styles, P. (2013). Induced seismicity and hydraulic fracturing for the recovery of hydrocarbons. *Marine and petroleum geology*, *45*, 171-185.

De Barros, L., Daniel, G., Guglielmi, Y., Rivet, D., Caron, H., Payre, X., ... & Gourlay, M. (2016). Fault structure, stress, or pressure control of the seismicity in shale? Insights from a controlled experiment of fluid−induced fault reactivation. *Journal of Geophysical Research: Solid Earth*, *121*(6), 4506-4522.

Deng, K., Liu, Y., & Harrington, R. M. (2016). Poroelastic stress triggering of the December 2013 Crooked Lake, Alberta, induced seismicity sequence. *Geophysical Research Letters*, *43*(16), 8482-8491.

Ellsworth, W. L., & Bulut, F. (2018). Nucleation of the 1999 Izmit earthquake by a triggered cascade of foreshocks. *Nature Geoscience, 11*(7), 531-535.

Evans, J. P., Forster, C. B., & Goddard, J. V. (1997). Permeability of fault-related rocks, and implications for hydraulic structure of fault zones. *Journal of structural Geology*, *19*(11), 1393-1404.

Eyre, T. S., Eaton, D. W., Garagash, D. I., Zecevic, M., Venieri, M., Weir, R., & Lawton, D. C. (2019a). The role of aseismic slip in hydraulic fracturing–induced seismicity. *Science advances*, *5*(8), eaav7172.

Eyre, T. S., Eaton, D. W., Zecevic, M., D'Amico, D., & Kolos, D. (2019b). Microseismicity reveals fault activation before M w 4.1 hydraulic-fracturing induced earthquake. *Geophysical Journal International*, *218*(1), 534-546.

Farrell, N. J. C., Healy, D., & Taylor, C. W. (2014). Anisotropy of permeability in faulted porous sandstones. *Journal of Structural Geology*, *63*, 50-67.

Fischer, A. D., Peng, Z., & Sammis, C. G. (2008). Dynamic triggering of high−frequency bursts by strong motions during the 2004 Parkfield earthquake sequence. *Geophysical Research Letters*, *35*(12).

Fu, Y., & Dehghanpour, H. (2020). How far can hydraulic fractures go? A comparative analysis of water flowback, tracer, and microseismic data from the Horn River Basin. *Marine and Petroleum Geology*, *115*, 104259.

Galloway, E., Hauck, T., Corlett, H., Pană, D., & Schultz, R. (2018). Faults and associated karst collapse suggest conduits for fluid flow that influence hydraulic fracturing-induced seismicity. *Proceedings of the National Academy of Sciences*, *115*(43), E10003-E10012.

Gao, D., & Kao, H. (2020). Optimization of the Match−Filtering Method for Robust Repeating Earthquake Detection: The Multisegment Cross−Correlation Approach. *Journal of Geophysical Research: Solid Earth, 125*(7), e2020JB019714.

Guglielmi, Y., Cappa, F., Avouac, J. P., Henry, P., & Elsworth, D. (2015). Seismicity triggered by fluid injection–induced aseismic slip. *Science*, *348*(6240), 1224-1226.

Haagenson, R., & Rajaram, H. (2020). Seismic diffusivity: The influence of fracture networks on the patterns of induced seismicity. In *EGU General Assembly Conference Abstracts* (p. 20308).

Hayward, T. W., & Bostock, M. G. (2017). Slip behavior of the queen Charlotte plate boundary before and after the 2012, MW 7.8 Haida Gwaii earthquake: evidence from repeating earthquakes. *Journal of Geophysical Research: Solid Earth*, *122*(11), 8990-9011.

Hunter, J. D. (2007). Matplotlib: A 2D graphics environment. *Computing in science & engineering*, *9*(3), 90-95.

Igarashi, T., Matsuzawa, T., & Hasegawa, A. (2003). Repeating earthquakes and interplate aseismic slip in the northeastern Japan subduction zone. *Journal of Geophysical Research: Solid Earth*, *108*(B5).

Igonin, N., Verdon, J. P., Kendall, J. M., & Eaton, D. W. (2020). Large−scale fracture systems are permeable pathways for fault activation during hydraulic fracturing. *Journal of Geophysical Research: Solid Earth*, e2020JB020311.

Jones, E., Oliphant, T., & Peterson, P. (2001). SciPy: Open source scientific tools for Python.

Kennett, B. L., Engdahl, E. R., & Buland, R. (1995). Constraints on seismic velocities in the Earth from traveltimes. *Geophysical Journal International*, *122*(1), 108-124.

Keranen, K. M., Savage, H. M., Abers, G. A., & Cochran, E. S. (2013). Potentially induced earthquakes in Oklahoma, USA: Links between wastewater injection and the 2011 Mw 5.7 earthquake sequence. *Geology*, *41*(6), 699-702.

King, G. C., Stein, R. S., & Lin, J. (1994). Static stress changes and the triggering of earthquakes. *Bulletin of the Seismological Society of America*, *84*(3), 935-953.

Kohli, A. H., & Zoback, M. D. (2013). Frictional properties of shale reservoir rocks. *Journal of geophysical research: solid earth*, *118*(9), 5109-5125.

Kozłowska, M., Brudzinski, M. R., Friberg, P., Skoumal, R. J., Baxter, N. D., & Currie, B. S. (2018). Maturity of nearby faults influences seismic hazard from hydraulic fracturing. *Proceedings of the National Academy of Sciences*, *115*(8), E1720-E1729.

Lei, X., Huang, D., Su, J., Jiang, G., Wang, X., Wang, H., ... & Fu, H. (2017). Fault reactivation and earthquakes with magnitudes of up to Mw4. 7 induced by shale-gas hydraulic fracturing in Sichuan Basin, China. *Scientific reports*, *7*(1), 1-12.

Lei, X., Wang, Z., & Su, J. (2019). The December 2018 ML 5.7 and January 2019 ML 5.3 earthquakes in South Sichuan basin induced by shale gas hydraulic fracturing. *Seismological Research Letters*, *90*(3), 1099-1110.

Li, A., & Richards, P. G. (2003). Using earthquake doublets to study inner core rotation and seismicity catalog precision. *Geochemistry, Geophysics, Geosystems*, *4*(9).

Li, L., Chen, Q. F., Niu, F., & Su, J. (2011). Deep slip rates along the Longmen Shan fault zone estimated from repeating microearthquakes. *Journal of Geophysical Research: Solid Earth*, *116*(B9).

Lockner, D. A., & Beeler, N. M. (1999). Premonitory slip and tidal triggering of earthquakes. *Journal of Geophysical Research: Solid Earth*, *104*(B9), 20133-20151.

Peña Castro, A. F., Roth, M. P., Verdecchia, A., Onwuemeka, J., Liu, Y., Harrington, R. M., ... & Kao, H. (2020). Stress Chatter via Fluid Flow and Fault Slip in a Hydraulic Fracturing‐Induced Earthquake Sequence in the Montney Formation, British Columbia. *Geophysical Research Letters*, *47*(14), e2020GL087254.

Rubinstein, J. L., & Mahani, A. B. (2015). Myths and facts on wastewater injection, hydraulic fracturing, enhanced oil recovery, and induced seismicity. *Seismological Research Letters*, *86*(4), 1060-1067.

Schaff, D. P., & Richards, P. G. (2004). Repeating seismic events in China. *Science*, *303*(5661), 1176-1178.

Schmittbuhl, J., Karabulut, H., Lengliné, O., & Bouchon, M. (2016). Long‐lasting seismic repeaters in the Central basin of the Main Marmara fault. *Geophysical Research Letters*, *43*(18), 9527-9534.

Schultz, R., & Wang, R. (2020). Newly emerging cases of hydraulic fracturing induced seismicity in the Duvernay East Shale Basin. *Tectonophysics*, 228393.

Schultz, R., Atkinson, G., Eaton, D. W., Gu, Y. J., & Kao, H. (2018). Hydraulic fracturing volume is associated with induced earthquake productivity in the Duvernay play. *Science*, *359*(6373), 304-308.

Schultz, R., Stern, V., Novakovic, M., Atkinson, G., & Gu, Y. J. (2015a). Hydraulic fracturing and the Crooked Lake sequences: Insights gleaned from regional seismic networks. *Geophysical Research Letters*, *42*(8), 2750-2758.

Schultz, R., Mei, S., Pană, D., Stern, V., Gu, Y. J., Kim, A., & Eaton, D. (2015b). The Cardston earthquake swarm and hydraulic fracturing of the Exshaw Formation (Alberta Bakken play). *Bulletin of the Seismological Society of America*, *105*(6), 2871-2884.

Schultz, R., Skoumal, R. J., Brudzinski, M. R., Eaton, D., Baptie, B., & Ellsworth, W. (2020). Hydraulic fracturing‐induced seismicity. *Reviews of Geophysics*, *58*(3), e2019RG000695.

Schultz, R., Stern, V., & Gu, Y. J. (2014). An investigation of seismicity clustered near the Cordel Field, west central Alberta, and its relation to a nearby disposal well. *Journal of Geophysical Research: Solid Earth*, *119*(4), 3410-3423.

Schultz, R., Wang, R., Gu, Y. J., Haug, K., & Atkinson, G. (2017). A seismological overview of the induced earthquakes in the Duvernay play near Fox Creek, Alberta. *Journal of Geophysical Research: Solid Earth*, *122*(1), 492-505.

Shen, L. W., Schmitt, D. R., & Schultz, R. (2019). Frictional stabilities on induced earthquake fault planes at Fox Creek, Alberta: a pore fluid pressure dilemma. *Geophysical Research Letters*, *46*(15), 8753-8762.

Stein, R. S. (1999). The role of stress transfer in earthquake occurrence. *Nature*, *402*(6762), 605-609.

Waldhauser, F., & Ellsworth, W. L. (2000). A double-difference earthquake location algorithm: Method and application to the northern Hayward fault, California. *Bulletin of the Seismological Society of America*, *90*(6), 1353-1368.

Wang, B., Harrington, R. M., Liu, Y., Kao, H., & Yu, H. (2020). A study on the largest hydraulic−fracturing−induced earthquake in Canada: Observations and static stress−drop estimation. *Bulletin of the Seismological Society of America*, *110*(5), 2283-2294.

Wang, B., Verdecchia, A., Kao, H., Harrington, R. M., Liu, Y., & Yu, H. (2021). A Study on the Largest Hydraulic Fracturing Induced Earthquake in Canada: Numerical Modeling and Triggering Mechanism. *Bulletin of the Seismological Society of America*.

Wang, R., & Küumpel, H. J. (2003). Poroelasticity: Efficient modeling of strongly coupled, slow deformation processes in multilayered half-space. *Geophysics*, *68*(2), 705-717.

Wang, R., Gu, Y. J., Schultz, R., Zhang, M., & Kim, A. (2017). Source characteristics and geological implications of the January 2016 induced earthquake swarm near Crooked Lake, Alberta. *Geophysical Journal International*, *210*(2), 979-988.

Warren-Smith, E., Fry, B., Kaneko, Y., & Chamberlain, C. J. (2018). Foreshocks and delayed triggering of the 2016 MW7. 1 Te Araroa earthquake and dynamic reinvigoration of its aftershock sequence by the MW7. 8 Kaikōura earthquake, New Zealand. *Earth and Planetary Science Letters*, *482*, 265-276.

Warren−Smith, E., Chamberlain, C. J., Lamb, S., & Townend, J. (2017). High−precision analysis of an aftershock sequence using matched−filter detection: The 4 May 2015 ML 6 Wanaka earthquake, Southern Alps, New Zealand. *Seismological Research Letters*, *88*(4), 1065-1077.

Weingarten, M., Ge, S., Godt, J. W., Bekins, B. A., & Rubinstein, J. L. (2015). High-rate injection is associated with the increase in US mid-continent seismicity. *Science*, *348*(6241), 1336-1340.

Wilson, M. P., Worrall, F., Davies, R. J., & Almond, S. (2018). Fracking: How far from faults?. *Geomechanics and Geophysics for Geo-Energy and Geo-Resources*, *4*(2), 193-199.

Wolhart, S. L., Harting, T. A., Dahlem, J. E., Young, T., Mayerhofer, M. J., & Lolon, E. P. (2006, January). Hydraulic fracture diagnostics used to optimize development in the Jonah field. In *SPE Annual Technical Conference and Exhibition*. Society of Petroleum Engineers.

Xu, C., Wang, J., Li, Z., & Drummond, J. (2010). Applying the Coulomb failure function with an optimally oriented plane to the 2008 Mw 7.9 Wenchuan earthquake triggering. *Tectonophysics*, *491*(1-4), 119-126.

Yamada, M., Mori, J., & Matsushi, Y. (2016). Possible stick−slip behavior before the Rausu landslide inferred from repeating seismic events. *Geophysical Research Letters, 43*(17), 9038-9044.

Yehya, A., Yang, Z., & Rice, J. R. (2018). Effect of fault architecture and permeability evolution on response to fluid injection. *Journal of Geophysical Research: Solid Earth*, *123*(11), 9982-9997.

Yu, H., Harrington, R. M., Liu, Y., & Wang, B. (2019). Induced seismicity driven by fluid diffusion revealed by a near−field hydraulic stimulation monitoring array in the Montney Basin, British Columbia. *Journal of Geophysical Research: Solid Earth*, *124*(5), 4694-4709.

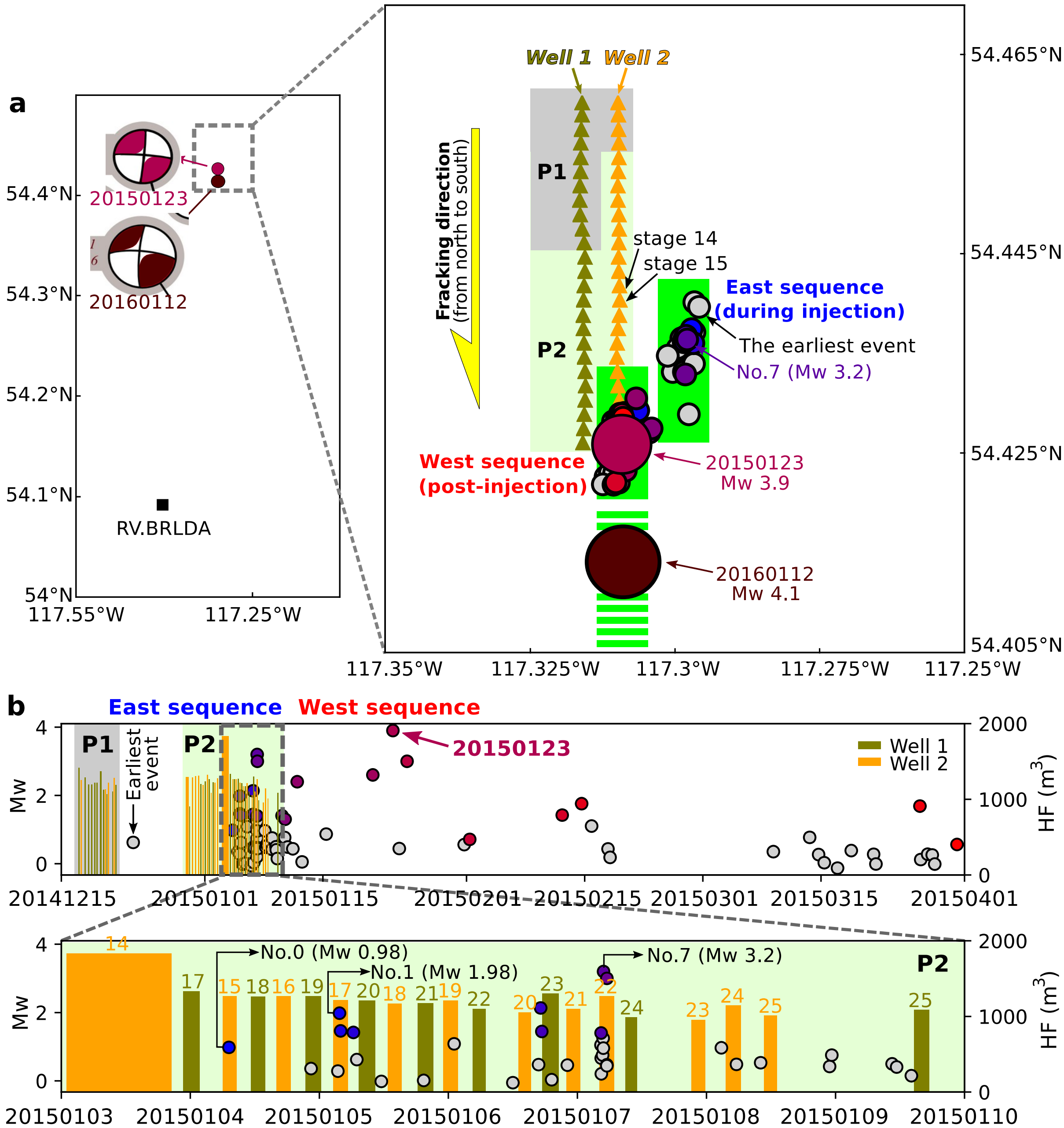

Figure 1. Comparison of induced seismicity and HF activity. (a), Location of the 2015 Mw 3.9 earthquake sequence in Fox Creek, Alberta, Canada. Beach balls of the 2015 Mw 3.9 and 2016 Mw 4.1 events are taken from prior work (*Schultz et al*., 2017). The black square in the left panel shows the seismic station used in this study. In the right panel, solid lime bars denote the two fault strands of the 2015 sequence; dashed lime bar marks the hosted fault of the 2016 Mw 4.1 event; triangles represent HF stages. (b), Injection history associated with the occurrence of induced earthquakes. The height of each colored bar represents the total volume of fluid injected at each stage while the width depicts the stage duration. In the bottom panel, stage ID is labelled above each treatment. In both (a) and (b), colored circles are the near-identical events (Figure 2); gray circles represent the uncorrelated small events; gray and pale green shaded areas represent P1 and P2 injection periods, respectively.

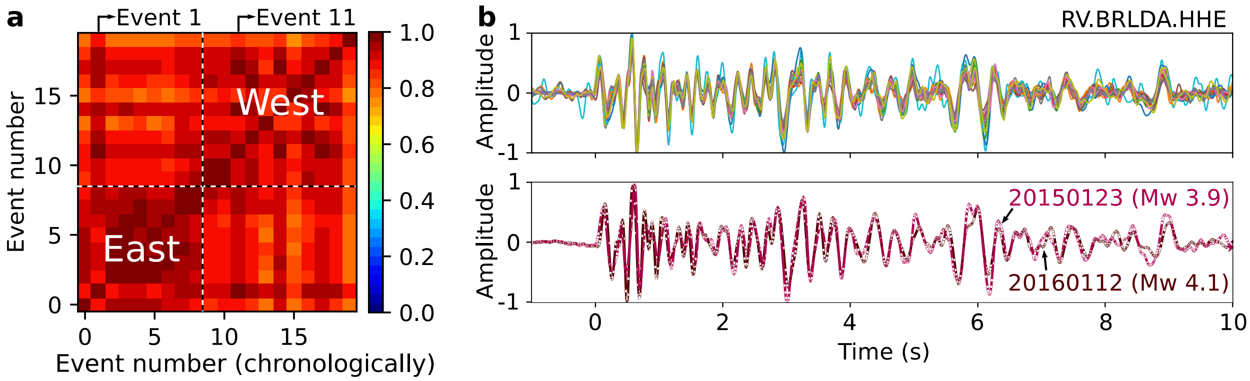

Figure 2. Identification of near-identical earthquakes. (a) Cross-correlation matrix of 20 correlated events (i.e., near-identical earthquakes). (b) Normalized waveforms of the 20 near-identical earthquakes (top panel) and of the two large events (bottom panel).

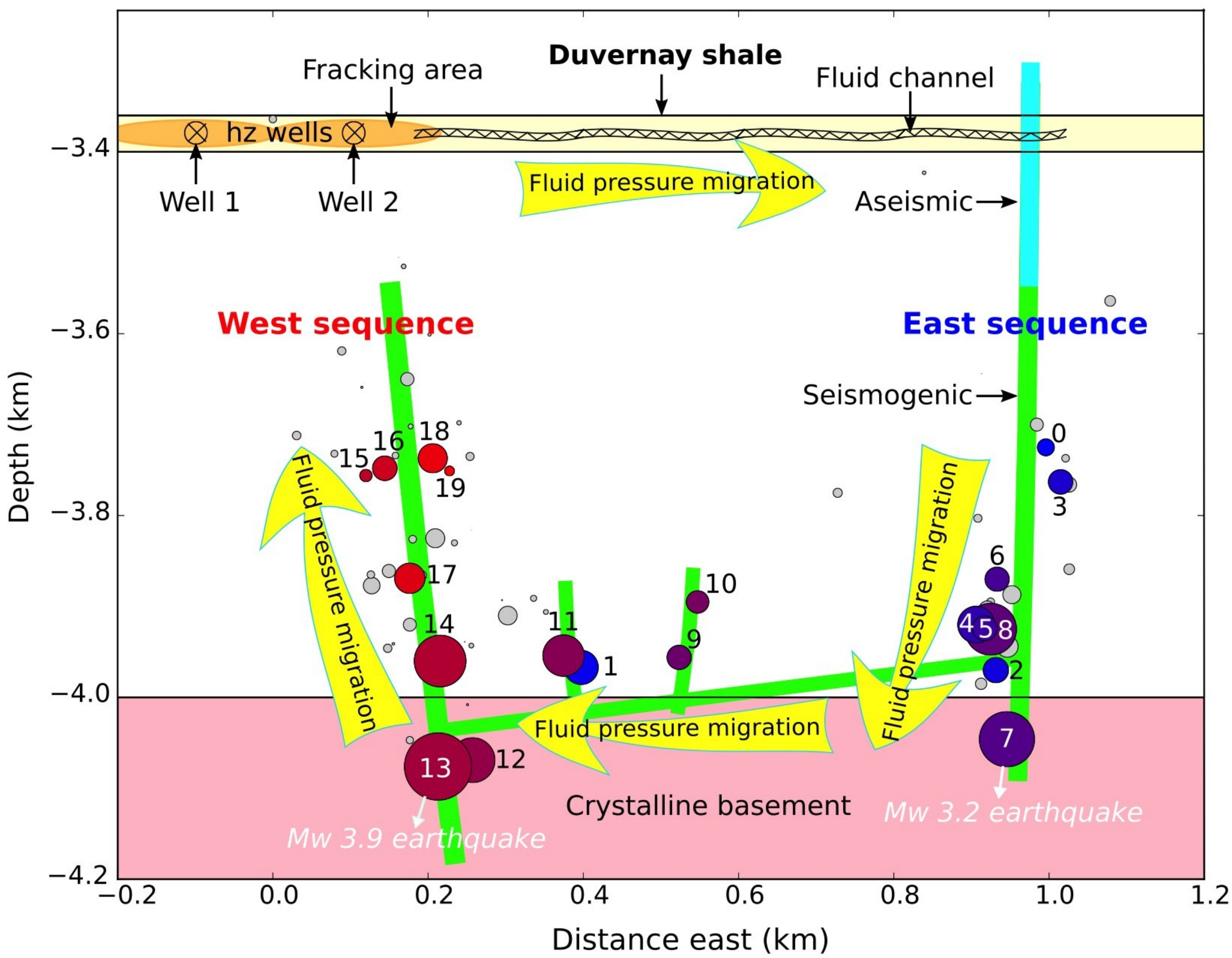

Figure 3. East-west cross section of the 2015 Mw 3.9 earthquake sequence. 20 correlated events are marked by numbered and color-coded circles, with the smaller numbers and cooler colors corresponding to earlier events. Gray circles represent the 49 poorly correlated events. Circle sizes are scaled according to earthquake magnitudes. Crossed circles mark two HF horizontal wells.

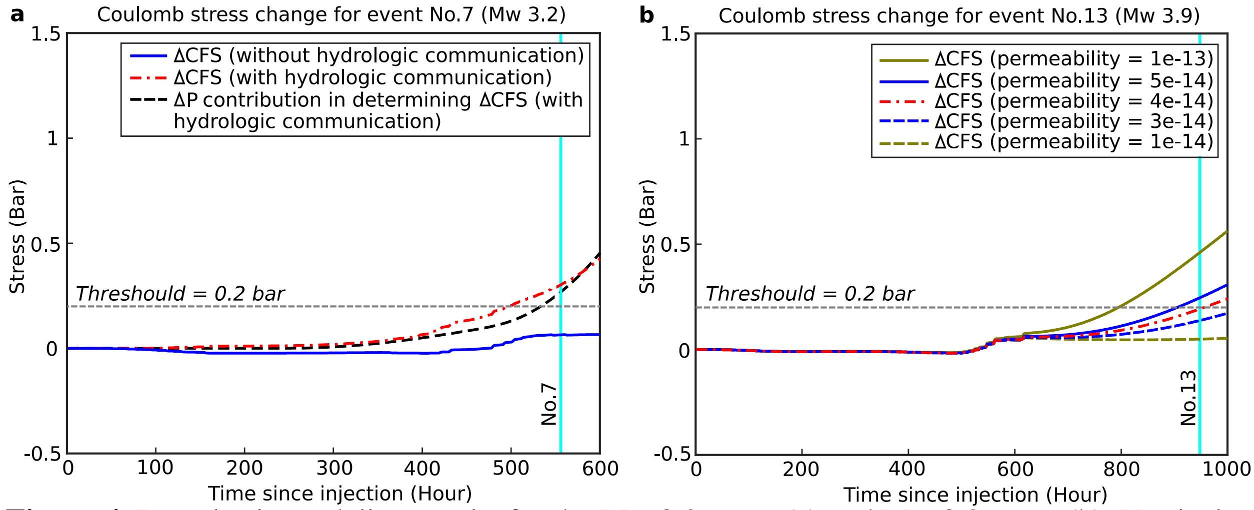

Figure 4. Poroelastic modeling results for the Mw 3.2 event (a) and Mw 3.9 event (b). Vertical cyan lines mark the origin times of the two earthquakes. Note for (b), the results of using a permeability lower than 1×10^{-14} m^2 are nearly identical to that of 1×10^{-14} m^2 and hence are not displayed for simplicity. In such low permeability cases, the ΔP contribution in determining the ΔCFS for the Mw 3.9 event is negligible as the fluid pressure can not reach the west sequence fault for the observed time scale. The corresponding ΔP contributions of using different permeabilities in (b) are given in Figure S2.

AGU PUBLICATIONS

Geophysical Research Letters

Supporting Information for

Complex 3D Migration and Delayed Triggering of Hydraulic Fracturing-Induced Seismicity

Dawei Gao[1,2], Honn Kao[1,2]*, Bei Wang[1,2], Ryan Visser[2], Ryan Schultz[3], Rebecca Harrington[4]

[1]School of Earth and Ocean Sciences, University of Victoria, Victoria, British Columbia, Canada.

[2]Pacific Geoscience Centre, Geological Survey of Canada, Sydney, British Columbia, Canada.

[3]Department of Geophysics, Stanford University, Stanford, CA, USA.

[4]Ruhr University Bochum, Institute of Geology, Mineralogy, and Geophysics, Bochum, Germany.

Contents of this file

Introduction

This Supporting Information provides additional texts, figures, and tables to further support the arguments and findings presented in the main text. Texts S1 and S2 present the technical details of CC calculation and poroelastic modeling, respectively. Figure S1 displays the histogram of the 49 poorly correlated small earthquakes. Figure S2 shows the ΔP contribution in determining the ΔCFS with different permeabilities for the Mw 3.9 event. Table S1 summarizes the solid and fluid properties of each layer used in the poroelastic model. Table S2 presents the injection data.

Text S1. Technical Details of CC Calculation

When performing the waveform cross-correlation, the seismic waveforms are band-pass filtered from 1 to 10 Hz (*Schmittbuhl et al.,* 2016; *Warren-Smith et al.*, 2017, 2018). The cross-correlation window is set to be 10 s, starting from 1 s before to 9 s after the theoretical predicted S-arrival (*Schultz et al*., 2017) based on the ak135 velocity model (*Kennett et al*., 1995). The choice of a 10-s window length is meant to capture the strongest and cleanest arrival and sufficient coda waves with a lower level of noise contamination. We do not choose a window starting from the P phase because the P waves are very small compared with the S phases, thus the result can be easily contaminated by noise (*Schultz et al*., 2017). The correlation is performed by sliding the waveform of one event from 4 s before the predicted S arrival of the other event to 4 s after, in one-sample increments. A ±4 s shift should be adequate to account for any predicted phase onset error due to an imperfect velocity model. The maximum value of the CC results during the sliding is defined as the final CC value of the event pair.

Text S2. Technical Details of Poroelastic Modeling

By assuming that the medium is homogeneous and isotropic, the evolution of pore pressure can be calculated by solving the coupled diffusion equations, as listed below (equivalent forms of the equations can be found in the literature, e.g., *Wang and Kumpel*, 2003),

$$\rho S \frac{\partial p}{\partial t} - \nabla \cdot \left(\rho \frac{\kappa}{\mu_d} \nabla p \right) = Q_m(x,t) - \rho \alpha \frac{\partial \varepsilon_{vol}}{\partial t} \tag{1}$$

$$S = \chi_f \theta + \chi_p (1-\theta) \tag{2}$$

$$q = -\frac{\kappa}{\mu_d} \nabla p \tag{3}$$

where ρ is the pore fluid density, S is the linearized storage parameter, p is the fluid pore pressure, κ is the permeability of the medium, μ_d is its dynamic viscosity, Q_m is the volumetric flow rate for a fluid source, α is the Biot-Willis coefficient, ε_{vol} is the volumetric strain of the porous matrix, χ_f is the compressibility of the fluid, χ_p is the compressibility of the rock, θ is the porosity, and q is the velocity variable which gives a volume flow rate per unit area of porous material. The governing equations for the poroelastic model are then given by:

$$-\nabla \cdot \sigma = F_v \tag{4}$$

$$\sigma_{ij} = \frac{2G\nu}{(1-2\nu)} \varepsilon_{kk} \delta_{ij} + 2G \varepsilon_{ij} - \alpha p \delta_{ij} \tag{5}$$

$$\varepsilon_{ij} = \frac{1}{2} ((\nabla \boldsymbol{u})^T + \nabla \boldsymbol{u}) \tag{6}$$

where σ is the stress tensor, F_v is the volume force vector (i.e., $F_v = (\rho\theta + \rho_b)g$, where g is the acceleration of gravity, and ρ_b is the bulk density), δ_{ij} is the Kronecker delta (equal to 1 when $i = j$, and to 0 when $i \neq j$), G is Young's modulus, ν is the Poisson's ratio, and $\boldsymbol{u}$ is the displacement vector.

We build a 3D model of 5 km × 10 km × 5 km in the x, y and z directions, respectively, and split the model into four simplified layers (Table S1). From top to bottom, the four layers correspond to the upper sedimentary section, the Duvernay shale formation in which the HF horizontal wells are located, the lower sedimentary section, and the crystalline basement (*Bao and Eaton*, 2016). The solid and hydrogeological properties of each layer are listed in Table S1. Within the model, we set the so-called roller condition as the side solid boundaries, i.e., no vertical movement is permitted for the solid material on the boundary. We then set the bottom and top solid boundaries as fixed and free surfaces, respectively. Next, we set the fluid boundaries to have no flow. In addition, at the top, we add a standard atmospheric pressure, and set the pore pressure at the top surface to 0. Finally, we set the original fluid condition to be hydrostatic equilibrium.

In our model, besides the stimulation points, we assume that the HF operations have created a fracture zone surrounding the horizontal wells (note that the fracture zone is confined in the Duvernay shale layer), leading to an increased permeability compared to the unfractured shale formation. The width of the fractures centered at the stimulation points is set to be 200 m. We assume the permeability of the fractures to be 5×10^{-15} m^2, the same as that of the fluid channel but three orders higher than the low-permeability unfractured shale formation (1×10^{-18} m^2, Table S1). As mentioned in the main text, there are two inferred fault systems, i.e., the east sequence fault and the west sequence fault. In the model, we create two near-vertical faults on the basis of the Mw 3.9 and Mw 3.2 mainshock and their aftershock locations. We also assume that there is a near-horizontal basement fault connecting the two vertical fault systems (Figure 3). We set the permeability along the fault surface for the two vertical faults to be three orders of magnitude larger than the confining rock (Table S1), as the fault damage zone could enhance the permeability (*Yehya et al*., 2018). For the near-horizontal fault, it is worth noting that we have tested multiple permeability values, ranging from the same as the surrounding rock ($1 \times 10^{-18}\ m^2$) to five orders larger than the surrounding rock ($1 \times 10^{-13}\ m^2$, Figure 4b). This range of permeability includes not only the scenario of a high-permeable horizontal fault, but also one where the horizontal fault does not exist.

To simulate the multi-stage fluid injection process, we assume that fluid is injected at a single point of each stage, and the consecutive stages migrate along the horizontal well bore. Each stage's fluid injection rate is the ratio between stage injection volume and duration time (calculated from Table S2). The outcomes (stress tensor and pore pressure change) from the poroelastic modeling are then used to calculate the ΔCFS as discussed in the main text.

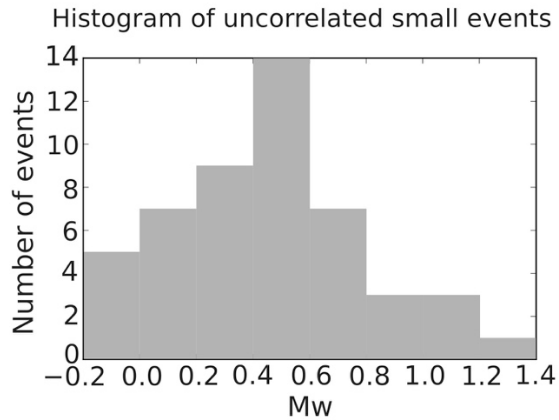

Figure S1. Histogram of the 49 poorly correlated small earthquakes.

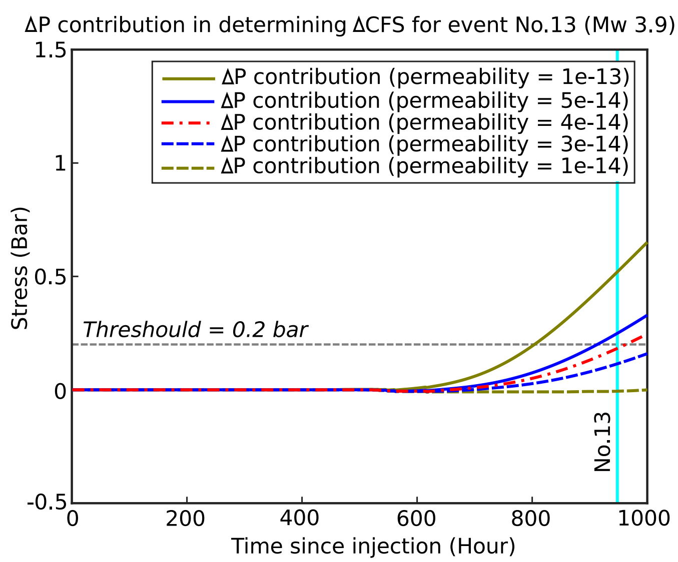

Figure S2. ΔP contribution in determining the ΔCFS for the Mw 3.9 event.

Table S1. Solid and fluid properties of each layer used in the model. Note that for the fracture zone, the permeability is 5×10^{-15} m^2 and the solid properties are the same as that of the confining Duvernay shale layer. For the two vertical faults, their solid properties are the same as the horizontal layers, and the permeability along the fault is 5×10^{-15} m^2.

	Layer 1	Layer 2 (HF layer)	Layer 3	Layer 4
Depth	0-3.3 km	3.3 km-3.4 km	3.4 km-4.1 km	4.1 km-5 km
Biot-Willis	0.7	0.7	0.7	0.7
P-wave velocity	5000 m/s	6100 m/s	6300 m/s	6900 m/s
S-wave velocity	2800 m/s	3520 m/s	3630 m/s	3983 m/s
Bulk Density (ρ_b)	2500 kg/m^3	2600 kg/m^3	2750 kg/m^3	2900 kg/m^3
Permeability	7.5×10^{-16} m^2	1×10^{-18} m^2	5×10^{-18} m^2	1×10^{-18} m^2
Porosity (θ)	0.1	0.05	0.05	0.08
Fluid density (ρ)	1000 kg/m^3	1000 kg/m^3	1000 kg/m^3	1000 kg/m^3
Fluid compressibility (χ_f)	4.5×10^{-10} Pa^{-1}	4.5×10^{-10} Pa^{-1}	4.5×10^{-10} Pa^{-1}	4.5×10^{-10} Pa^{-1}
Fluid dynamic viscosity (μ_d)	0.79×10^{-3} Pa*s	0.79×10^{-3} Pa*s	0.79×10^{-3} Pa*s	0.79×10^{-3} Pa*s

Table S2. Injection data.

Well	Stage	Stage-start	Stage-end	Total Fluid (m^3)
1	1	17-12-2014--00:38	17-12-2014--04:02	1417
1	2	17-12-2014--18:08	17-12-2014--21:30	1288
1	3	18-12-2014--04:17	18-12-2014--07:10	1196
1	4	18-12-2014--13:53	18-12-2014--16:31	1196
1	5	18-12-2014--21:37	19-12-2014--00:11	1220
1	6	19-12-2014--04:50	19-12-2014--07:25	1217
1	7	19-12-2014--14:30	19-12-2014--18:47	1367
1	8	19-12-2014--23:44	20-12-2014--02:16	1123
1	9	20-12-2014--08:46	20-12-2014--11:01	1065
1	10	21-12-2014--00:33	21-12-2014--02:50	1101
1	11	21-12-2014--10:23	21-12-2014--13:36	1189
1	12	30-12-2014--03:43	30-12-2014--06:00	907.4
1	13	31-12-2014--11:45	31-12-2014--14:23	1199
1	14	31-12-2014--23:28	01-01-2015--02:26	1234
1	15	01-01-2015--11:35	01-01-2015--14:20	1266
1	16	01-01-2015--22:40	02-01-2015--01:34	1226
1	17	03-01-2015--22:43	04-01-2015--01:45	1333
1	18	04-01-2015--11:17	04-01-2015--13:56	1265
1	19	04-01-2015--21:24	05-01-2015--00:21	1268
1	20	05-01-2015--07:21	05-01-2015--10:26	1210.7
1	21	05-01-2015--18:17	05-01-2015--21:10	1174
1	22	06-01-2015--04:29	06-01-2015--06:55	1102
1	23	06-01-2015--17:30	06-01-2015--20:33	1301
1	24	07-01-2015--08:54	07-01-2015--11:05	987
1	25	09-01-2015--14:35	09-01-2015--17:26	1084
2	1	17-12-2014--06:52	17-12-2014--10:44	1253
2	2	20-12-2014--03:56	20-12-2014--07:00	1128
2	3	20-12-2014--13:06	20-12-2014--15:55	1219
2	4	21-12-2014--04:44	21-12-2014--07:21	1282
2	5	29-12-2014--17:52	30-12-2014--01:40	1294

2	6	30-12-2014--11:45	30-12-2014--14:36	1290
2	7	30-12-2014--20:26	30-12-2014--23:11	1305
2	8	31-12-2014--04:33	31-12-2014--07:20	1309
2	9	31-12-2014--17:58	31-12-2014--20:53	1192
2	10	01-01-2015--06:03	01-01-2015--08:49	1324
2	11	01-01-2015--16:46	01-01-2015--19:02	1087
2	12	02-01-2015--03:29	02-01-2015--06:18	1219
2	13	02-01-2015--10:36	02-01-2015--13:19	1278
2	14	03-01-2015--00:58	03-01-2015--20:28	1834
2	15	04-01-2015--06:01	04-01-2015--08:39	1267
2	16	04-01-2015--16:04	04-01-2015--18:42	1266
2	17	05-01-2015--02:36	05-01-2015--05:20	1218
2	18	05-01-2015--12:44	05-01-2015--15:17	1171
2	19	05-01-2015--23:03	06-01-2015--01:45	1212
2	20	06-01-2015--13:02	06-01-2015--15:22	1056
2	21	06-01-2015--21:58	07-01-2015--00:35	1101
2	22	07-01-2015--04:03	07-01-2015--06:49	1267
2	23	07-01-2015--21:09	07-01-2015--23:45	957
2	24	08-01-2015--03:35	08-01-2015--06:26	1144
2	25	08-01-2015--10:42	08-01-2015--13:04	1010

124